ASME Journal of Manufacturing Science and Engineering
Online journal at:
https://asmedigitalcollection.asme.org/manufacturingscience

Yang Yang
Center for Advanced Manufacturing,
University of Southern California,
Los Angeles, CA 90007
e-mail: yyang088@usc.edu

Ying Cai
Center for Advanced Manufacturing,
University of Southern California,
Los Angeles, CA 90007
e-mail: yingcai@usc.edu

Yeo Jung Yoon
Center for Advanced Manufacturing,
University of Southern California,
Los Angeles, CA 90007
e-mail: yeojungy@usc.edu

Hangbo Zhao
Center for Advanced Manufacturing,
University of Southern California,
Los Angeles, CA 90007
e-mail: hangbozh@usc.edu

Satyandra K. Gupta[1]
Center for Advanced Manufacturing,
University of Southern California,
Los Angeles, CA 90007
e-mail: guptask@usc.edu

Sensor-Based Planning and Control for Conformal Deposition on a Deformable Surface Using an Articulated Industrial Robot

Robotic manipulators can be used to deposit materials on non-planar surfaces. Conventional sensor-based industrial robots can only work on stationary surfaces, relying on the scanned data prior to printing. As a result, performing depositions that involve changes in plane motion presents significant challenges. The deposition of conformal materials on a time-varying deformable surface requires the manipulators to update coordinates in real time on the plane for positioning and orientation. This can be achieved by employing multiple sensors for manipulator motion planning and control, in order to prevent collisions between the tool and the surface. In this paper, we propose simple tool center point calibration, initial point coordinate estimation, and a gap compensation scheme to combine real-time feedback control and direct conformal deposition. Combining these elements allows us to maintain a controlled gap between the tooltip and the deformable surface during the deposition. We test the efficacy of the proposed approach by printing a single layer of ink patterns with approximately 950 μm line width on a deformable surface. We also characterize the printing quality with different gaps and printing steps and show that sensor-based control is critical in smooth printing. Finally, the effects of changing the relative position of the tooltip, different surface colors, and laser sensor position are characterized.
[DOI: 10.1115/1.4063560]

Keywords: robotic manipulator, conformal printing, sensor-based planning, additive manufacturing

1 Introduction

Material extrusion is one of the most popular additive manufacturing (AM) processes [1]. In conventional extrusion-based AM, material deposition is performed on planar, horizontal surfaces. Due to this planar material deposition configuration, printing a curved geometry requires stacking multiple planar layers by approximating the desired geometry. However, this could lead to poor shape approximation, staircase effect, and anisotropic mechanical properties due to the presence of layer interfaces. The use of robots in material extrusion-based AM can overcome some of these limitations, thereby significantly expanding the capabilities of AM processes. Robots enable conformal deposition instead of using planar horizontal layers [2–6]. In our previous work, conformal deposition using robots enables direct printing on three-dimensional (3D) surfaces with multi-resolution nozzles [7]. The use of robots also enables printing over prefabricated components that have been inserted during the AM process [8]. We also realized material deposition at mesoscale on curved surfaces using an industrial robot [9]. Figure 1 highlights two examples of extrusion-based conformal 3D printing processes using robotic manipulators, including fused deposition modeling (FDM) and direct ink writing (DIW) processes.

Conformal material deposition can be achieved using a three degrees-of-freedom (DOF) gantry-based system which enables accurate positioning of a deposition tool. However, fixed tool orientation in such 3DOF gantry-based systems may lead to unsuccessful or poor-quality printing due to varying angles between the deposition tool and the target surface. Additionally, printing complex parts may require the adjustment of tool orientations to avoid collision between the tooltip and the printed part [10–12]. To satisfy these requirements, we consider a 6-DOF manipulator for the extrusion-based AM process. A robotic manipulator with six or more DOF can be used to control the position and orientation of the deposition tool during material deposition. This accurate positioning and flexible control enable material deposition on non-planar surfaces. Maintaining an appropriate gap between the tooltip and the surface is crucial for avoiding collisions and ensuring high printing quality. Excessively large gaps can result in inaccurate material placement, while insufficient gaps can lead to undesired material accumulation or even unsuccessful material extrusion out of the printing tooltip, potentially causing tooltip clogging. To maintain an optimal gap between the tooltip and the surface, sensor-based planning of material deposition is necessary.

In this paper, we present conformal deposition on a deformable surface with sensor-based planning and control. We use a 6-DOF

[1]Corresponding author.
Manuscript received May 12, 2023; final manuscript received September 17, 2023; published online October 19, 2023. Assoc. Editor: Cheryl Xu.

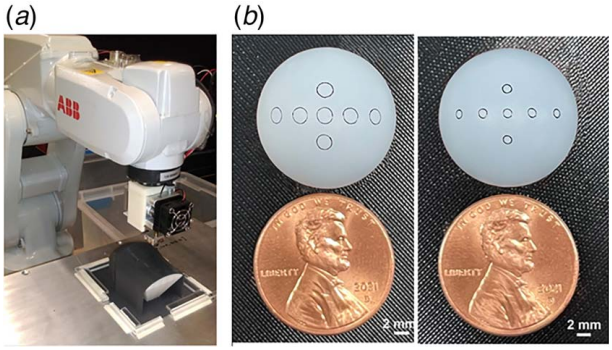

Fig. 1 Examples of conformal 3D printing on non-planar surfaces using a robot arm: (*a*) FDM-based printing on curved surfaces using a 6-DOF manipulator [2] and (*b*) DIW of mesoscale ink patterns on spherical surfaces [9]

manipulator and multiple sensors including a laser displacement sensor (LDS) and cameras to realize in situ material deposition on a deformable and moving surface. The motors are controlled to generate random motion of the deformable surface. The gap compensation and the control of the tooltip should be instantly executed when the sensors capture the motions of the deformable surface. Our work includes the correct registration between the target non-planar surface and the robot frame as well as the registration of the deposition tool with respect to the robot frame. Tool and robot calibration are required for our work. In this paper, we present the details of the gap compensation scheme that enables accurate positioning of the tooltip with respect to the deformable surface. Our gap compensation scheme enables us to maintain an appropriate gap between the tooltip and the underlying surface. We test the efficacy of our proposed approach by printing several types of patterns on non-planar and non-stationary substrates. Finally, we characterize the gap variation to evaluate the proposed approach. We believe conformal material deposition will be highly useful in various applications including electronics, energy, and healthcare fields. For example, Fig. 2 shows the in situ 3D printing process of biomedical devices including hydrogel-based sensors on deformable surfaces such as human organs using an adaptive 3D printing system [13].

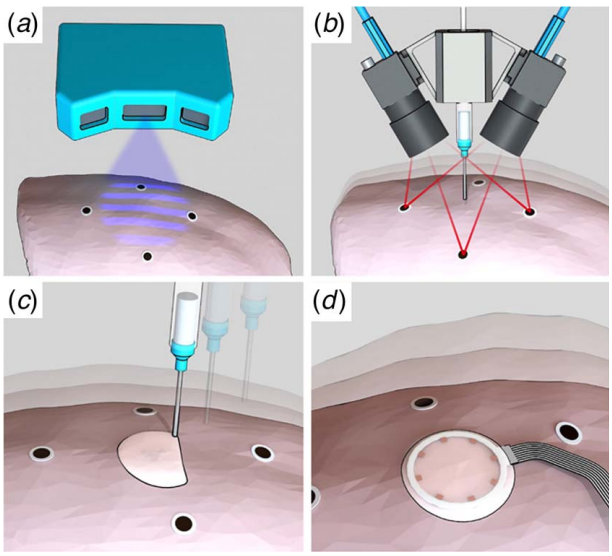

Fig. 2 An illustrative example of printing on deformable surfaces: (*a*) scanning the lung surface, (*b*) tracking the motion of the moving lung surface due to breathing, (c) in situ 3D printing of hydrogel ink on the lung surface, and (*d*) in situ monitoring of the lung surface movement using the printed sensor [13]

In our paper, we show that a robotic 3D printing system enables conformal material deposition on a curved, deformable, and moving surface. The structure of this paper is as follows: in Sec. 3, we describe the experimental setup used to realize in situ material deposition on a deformable surface. We describe the general approach including tool center point calibration, initial point coordinate estimation, and real-time gap compensation in Sec. 4. The experimental results and conclusions are shown in Secs. 5 and 7, respectively.

2 Related Work

The incorporation of robots into smart manufacturing processes has become increasingly popular in recent years, owing to their potential to improve quality and flexibility [14]. These technologies are being utilized across a diverse range of manufacturing processes, including sanding, finishing, spray painting, material assembly, 3D printing, and more [15–24]. 3D printing is one of those processes, and a robot enables printing on complex surfaces. The field of 3D printing has been widely studied due to its promising applications in numerous fields, such as material assembly, flexible electronics, and biomedical engineering.

Previous work is mostly focused on 3D printing on static surfaces, with demonstrations such as 3D printing electrical antennas on convex and concave surfaces of a glass hemisphere [25], bacteria-derived materials on a doll face [26], microfluidic channels on a spherical surface [27], robotic multi-resolution conformal printing [7,28], and robotic mesoscale conformal printing on hemispherical surfaces [9]. These studies rely on known geometries of the target surfaces prior to printing, either by printing on well-defined geometries or through the sensor measurement. Due to the complexity of printing surfaces, good printing results also require high precision of actuators, changing tooltip's direction, and efficient path planning.

More recently, conformal 3D printing has been demonstrated on movable or deformable surfaces. Johnson et al. used a Leap Motion sensor to apply the ink to a stationary mannequin hand in the desired M pattern, which can achieve coverage of 31,366 of the desired 36,630 pixels (85.6%) [29]. They also proved that this system can work for a free-moving human hand. However, no error analysis was executed after printing on the moving hand. Other than the Leap Motion sensor, O'Neill et al. used a projected line green laser and monocular camera to obtain the depth information of the moving hand for multi-layer deposition [30]. The printed 3D multi-layer structures have a 1.6 mm average error of the layer height and 87.8% volumetric accuracy. Our system allows for more precise deposition by accurately controlling the gap between a tooltip and a deformable surface.

Zhu et al. reported an adaptive system with a light scanner and multiple cameras to realize direct ink writing of functional materials on moving freeform surfaces, such as moving human hands, live mice, porcine lungs, and deformable phantom faces (see Fig. 3) [13,31]. In the system they proposed, the error of visual tracking was under 1.5 mm on target surfaces exhibiting slow motion (<8 mm/s). However, the sensor-based control approach presented in this study requires scanning the substrate to get an initial model, increasing the process complexity. In their study [32], they also discussed artificial intelligence (AI)-empowered 3D printing approaches on movable surfaces. 3D printing on deformable surfaces has more challenges than that on static surfaces. Among them, maintaining the gap between the tooltip and the movable surface is essential since it is the key to depositing materials uniformly and continuously without collisions. An efficient way to maintain the gap is to introduce a feedback control system [13,29–31] equipped with sensors such as cameras and 3D scanners. These sensors, either employed individually or in a multi-sensor configuration, play an essential role in enabling 3D printing on movable or deformable surfaces, as shown in these studies [13,29–31]. Besides, AI can play an important role in the real-time adaptation

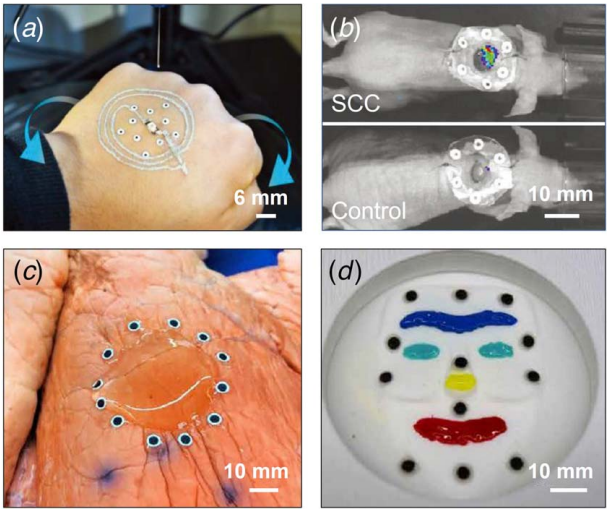

Fig. 3 Examples of 3D printing on movable or deformable surfaces: (*a*) 3D printing of an inductive coil on a moving hand [31], (*b*) 3D printing of a squamous cell carcinoma green fluorescent protein/Luciferase line (top) on a live mouse and the control group (bottom) [31], (*c*) 3D printing of a circular layer of hydrogel on a porcine lung [13], and (*d*) 3D printing of shapes of eyebrows, eyes, nose, and mouth on a phantom face [13]

to changes in the operation environment, such as ink-flow control, printing drawbacks, and deformation of the surface [32].

Finally, as described in Refs. [13,30,31], O'Neill et al. and Zhu et al. used low DOF gantries to explore the 3D printing systems for the movable or deformable surfaces. Despite their capabilities of printing on complex surfaces, such types of gantries have limitations of introducing poor shape approximation, staircase effect, and anisotropic mechanical properties due to the presence of layer interfaces. These restrictions can be released by using 6-DOF articulated industrial manipulators, which can increase the printing accuracy by adjusting the tooltip to be normal to the complex surface and depositing curved layers [33]. Hence, various examples of 6-DOF robotic 3D printing have been reported. Kraljic and Kamnik have presented an approach to curved layer slicing [33]. Bhatt et al. have studied robotic multi-resolution conformal printing [7,28] and multi-axis wire arc additive manufacturing [34]. Shembekar et al. have studied generating tool paths for the non-planner printing surface [2]. The authors presented the proper robot trajectories for the 6-DOF manipulator to avoid collisions between a nozzle tip and a curved surface. Holness et al. presented a novel 3D printing technique to create conductive polyaniline structures [35]. The 3D conductive structures are made using a robot-controlled platform with conductive polymer-based sensors and actuators. Many other studies of robotic 3D printing processes can be found in Refs. [36–38].

To our knowledge, research efforts in this area have been largely focused on printing functional materials on a static surface using low DOF gantries. There has been a lack of quantitative studies on how to improve printing accuracy when printing on a non-stationary and deformable surface. Our paper will study how to use a 6-DOF manipulator to perform 3D printing on a deformable surface with sensor-based planning and control. It will focus on how to improve printing accuracy by precisely controlling the gap between a tooltip and deformable surface.

3 Experimental Setup

Figure 4 shows the experimental setup used in this study. The model of the articulated industrial manipulator used is Yaskawa Motoman GP8. It is a 6-DOF manipulator with an 8 kg payload, 727 mm horizontal reach, 1312 mm vertical reach, and a

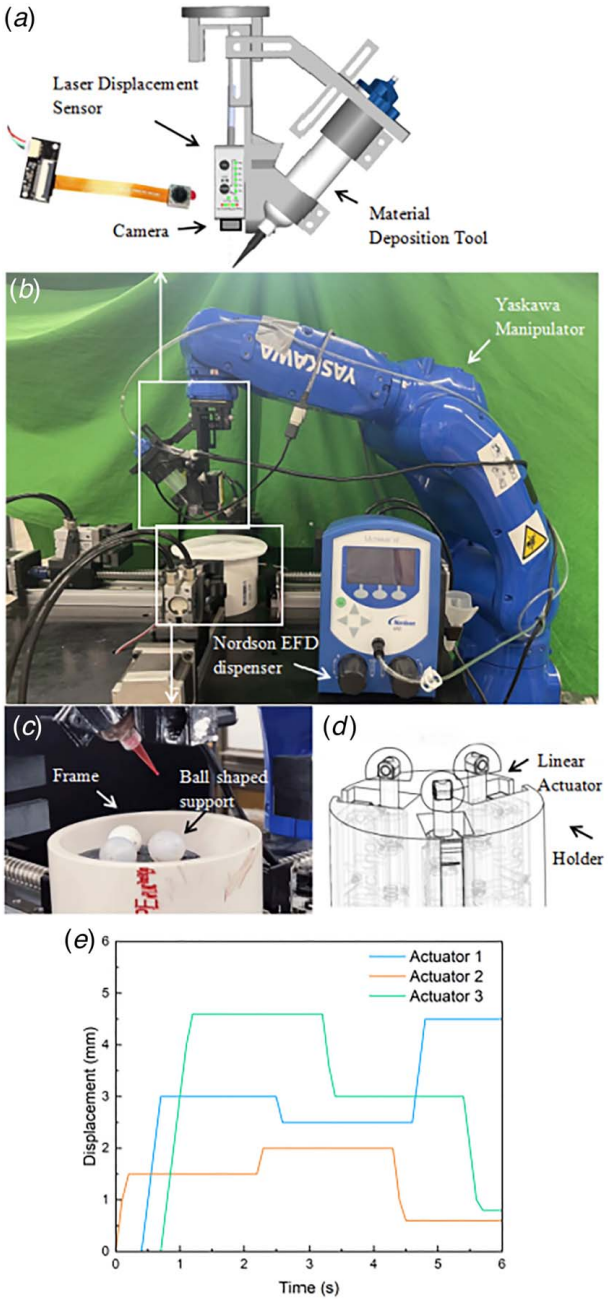

Fig. 4 Experimental setup for robotic conformal 3D printing: (*a*) computer-aided design model for the material deposition tool and sensors, (*b*) overview of the entire experimental setup, (*c*) and (*d*) components of the test bed, and (*e*) programmed displacements of the three actuators as a function of time

repeatability of 0.01 mm. The Yaskawa manipulator can be controlled by the YRC 1000 microcontroller. Its applications in the industry include handling, assembly, pick and place, and quality testing [18]. The manipulator is selected for the experiments because of its high repeatability. Also, considering its size and reachability, this robot should be placed close to the target object so that it can provide the flexibility to perform conformal printing.

Two types of sensors are used in the experimental setup. The first type of sensor is the auto-focus USB camera module (Sensor OV5640, Bewinner, Beijing, China). This compact sensor can be installed on industrial equipment to provide adequate quality for image processing. The camera is used for the tool center point (TCP) calibration. The process of TCP calibration is described

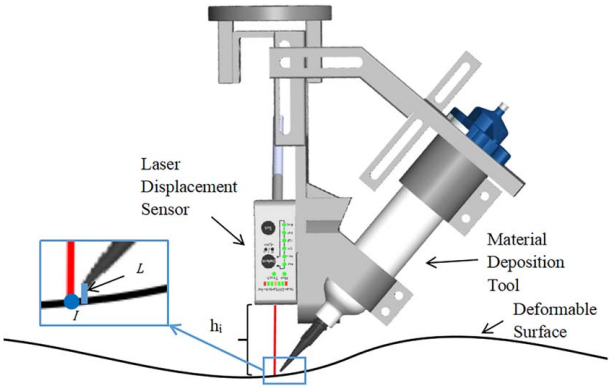

Fig. 5 Schematic illustration of the placement of the laser displacement sensor for gap compensation. The solid line from the LDS to the surface represents the laser beam. (Color version online.)

further in Sec. 4.1. The second type of sensor is the LDS. The model is LDS Optex CD33-30N-422 with a measurement range of 30 mm $\pm$4 mm and repeatability of 2 μm. This LDS is used for the gap compensation described in Sec. 4.3.

The test bed for the deformable surface consists of a silicone membrane (approximately 1.25 mm in thickness). The boundary of the silicone membrane is clamped to a circular frame. A mechanism is placed underneath the silicone surface to deform the surface vertically. The mechanism consists of three 3D-printed rigid plastic supports and three microlinear actuators (PQ12-R, Actuonix Motion Devices, Saanichton, BC, Canada) with three ball-shaped supports attached at the top. The actuators are controlled by an Arduino board (Uno Rev3, Somerville, MA). The time interval for each pulse of the linear actuators and the changes in height are set to be random. Throughout the entire process of retraction and extension, the actuators move at an average velocity of approximately 1 mm/s, reaching a maximum displacement of 5 mm. Figure 4(*e*) presents the displacements of the three actuators during the experiment, as determined by the program settings and pulse values. The membrane is prepared by mixing platinum-catalyzed silicone (Ecoflex 00–30, Smooth-On, Macungie, PA) with 3 wt% of white silicone pigments (Silc Pig, Smooth-On, Macungie, PA) inside a mold and curing at room temperature for 4 h.

Platinum-catalyzed silicone (Ecoflex 00–30, Smooth-On, Macungie, PA) with a viscosity of 3000 cps is used as the base material for the ink. A thixotropic agent (THI-VEX, Smooth-On, Macungie, PA) with 3 wt% is added to increase the ink viscosity. A brown silicone pigment (Silc Pig, Smooth-On, Macungie, PA) with 3 wt% is added for better visualization. The mixture is thoroughly mixed in a planetary centrifugal mixer (Thinky ARE-310, Laguna Hills, CA) for 30 s and deposited within Ecoflex 00–30's pot life (45 min) using a pneumatic fluid dispenser (Ultimus II, Nordson EFD, Westlake, OH) through a printing syringe with a fluid dispensing precision tip (Nordson EFD, Westlake, OH; inner diameter: 0.01 in). The syringe is mounted at 45 deg angle with respect to the LDS, at which angle it does not cause a collision with the surface.

4 Approach

To realize conformal printing on a deformable, non-planar surface using the manipulator, we first perform the TCP calibration as described in Sec. 4.1. During the TCP calibration, we obtain the relative position of the tooltip and the laser point projected from the LDS. Section 4.2 describes how to identify the coordinates (with respect to the base coordinate system) of the tooltip starting point for the deposition. In Sec. 4.3, we explain how to compensate for the gap between the tooltip and the deformable surface in real-time to reduce gap errors.

First, we drive the manipulator to the preparation bench to install the experimental tools. The manipulator is then moved to the desired position, where the gap between the tooltip and the surface of the preparation bench is small enough to just allow ink extrusion. The relative position of the laser point and the tooltip is recorded by the camera detector (Fig. 6(*a*)). This process is referred to as the preparation step.

4.1 Tool Center Point Calibration. The tooltip is set as the TCP. To calibrate the TCP, we localize the relative position of the printing tip and the laser point with respect to the robot base frame. The robot base frame is located on the base link of the manipulator, while the base link is mounted to the ground. This calibration is enabled by using a camera positioned on the LDS (Fig. 4). In the setup, the LDS is approximately placed at the center of the flange and perpendicular to it. Therefore, it can be approximated that the laser point is at the center of the flange. The tooltip is simultaneously monitored in this camera. We calibrate the TCP using the following steps:

(1) The image taken in the preparation step needs to be processed to find the position of the laser point and the tooltip, based on which we can calculate the distance to determine whether to change the position and plan the subsequent path.
(2) For the laser point position determination, it is necessary to adjust the brightness of the spot image and perform denoising preprocessing first. The image is then thresholded and converted to a binary image (Fig. 6(*b*)). The pixel intensity of the binary image can be approximated by a two-dimensional Gaussian function (Fig. 6(*c*))

$$f(x, y) = A \exp\left(-\frac{(x - x_o)^2}{2\sigma_x^2} - \frac{(y - y_o)^2}{2\sigma_y^2}\right) \quad (1)$$

where A is the peak intensity of the Gaussian distribution, x_o and y_o are the central coordinates in the x and y directions, respectively, σ_x and σ_y are the standard deviations in the x and y directions, respectively. Since the spot image has

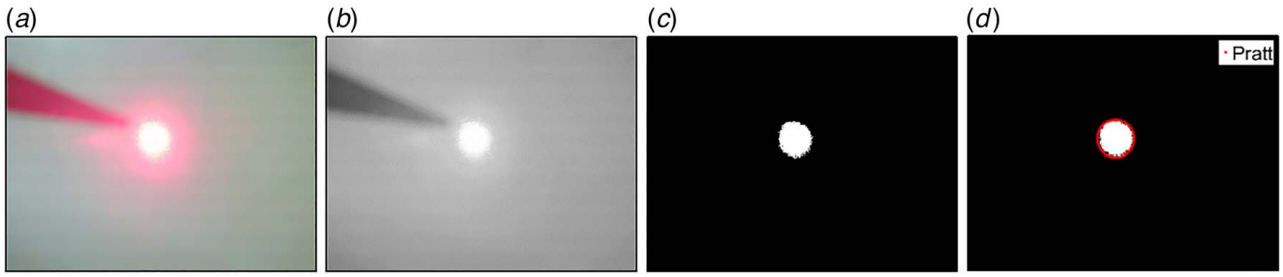

Fig. 6 Image processing for the laser spot detection: (*a*) original image, (*b*) binary image, (c) image after applying a two-dimensional Gaussian function, and (*d*) image with the laser spot outline using a Pratt circle fitting method (Color version online.)

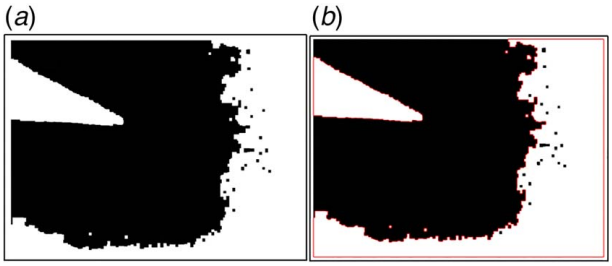

Fig. 7 Image processing for the tooltip: (*a*) image processed into a simple binary graph and (*b*) edge extraction for the tip position

large noises, we then use the non-iterative fast center fitting method proposed by Pratt for center fitting [39] as shown in Fig. 6(*d*). This method is essentially a least square center fitting method with the general equation of a circle as the objective function.

(3) For the tooltip position determination, the image still needs to be processed into a simple binary graph first (Fig. 7(*a*)). Then we can extract the edge of the image to find the tip position (Fig. 7(*b*)). The tooltip position plays an important role in determining the manipulator path and ensuring that the LDS reading reflects the surface status, which is discussed in Sec. 5.

(4) In the final step, the distance between the laser point and the tooltip can be calculated based on the processed image and the relative position can be determined. For better results, the distance should be less than 1 mm so that the position of the tooltip can be approximated to be one of the laser points when performing the compensation in Sec. 4.3.

The position of the tooltip relative to the laser point is known by the TCP calibration. Thus, the tip trajectory is first defined by using the relative positions and the flange trajectory can be calculated based on the relative position.

4.2 Initial Point Coordinate Estimation. The initial point is defined as the point at which printing starts. To determine the initial point coordinates, we detect the size of the laser point in the camera at different positions. The area of the spot in Fig. 6(*d*) is first calculated based on the circle fitted using the Pratt method, referred to as A_i. Under the same conditions, the size of the object in the image is related to the distance from which the image was captured, hence the location can be determined by comparing the sizes of the images. Before the estimation, the manipulator is driven over the test bed and an image is taken for comparison with A_i for every millimeter it moves down until the image size is within the range of $(A_i \pm 50)$ pixels. The Z coordinate size of the manipulator at this position is recorded and set as the Z coordinate of the initial point. At the same time, the X and Y coordinates are recorded and used as the starting point to calculate the two-dimensional model coordinates of the pattern to be printed.

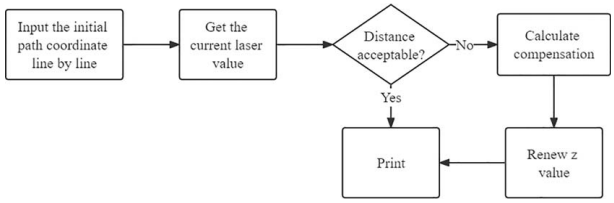

Fig. 9 Flowchart indicating the steps in the gap compensation process

4.3 Real-Time Gap Compensation. After the TCP calibration and the initial point coordinate determination, we try to drive the manipulator to deposit ink materials. Since the surface is set to be deforming in real-time, the gap between the tooltip and the substrate surface needs to be compensated to avoid the tooltip hitting the surface and to ensure continuous ink deposition. It is assumed that the X and Y coordinates of the manipulator have been calculated by MATLAB according to the graphic features to be printed, and only the vertical motion along the Z-axis needs to be compensated. We can perform compensation based on the real-time Z coordinate instead of acquiring the 3D point cloud coordinates of the plane. In this section, we propose a method for real-time gap compensation using an LDS mounted near the tooltip. Figure 9 illustrates the flowchart of the gap compensation process.

In Fig. 5, Point ***I*** is the intersection of the LDS's laser beam and the extension line of the tooltip's axis. The vertical distance between the end of the tooltip and the substrate is l, which is the gap that needs to be maintained. To compensate for the gap variation during printing, the LDS is utilized to scan the surface. The value obtained by the laser sensor is the distance in the Z-axis direction, recorded as h_i, and the laser value detected in the preparation step is recorded as h_0. The compensation is calculated as the difference between h_i and h_0. The positive or negative value of the result represents whether the manipulator is going straight up or down. Based on the result calculated in real-time, the manipulator is driven to fine-tune the tooltip's position.

When generating the compensated path by independently varying the tooltip's position along the tooltip's axis over the path, the final Z coordinate can be calculated based on the Z coordinate of the previous point, and the compensation calculated using Eq. (2)

$$z_i = z_{i-1} - (h_i - h_0) \tag{2}$$

where i is a positive integer, representing the order of the points; z_{i-1} and z_i denote the Z coordinates of the previous and current points,

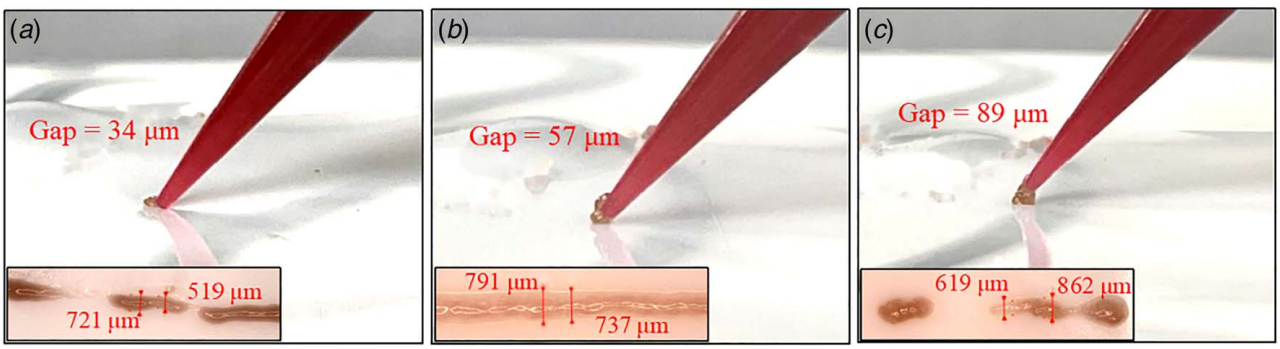

Fig. 8 Angled-view images of different gaps between the tooltip and the deformable surface, and the corresponding printed lines (insets). The gaps in (*a*), (*b*), and (*c*) are 34 μm, 57 μm, and 89 μm, respectively.

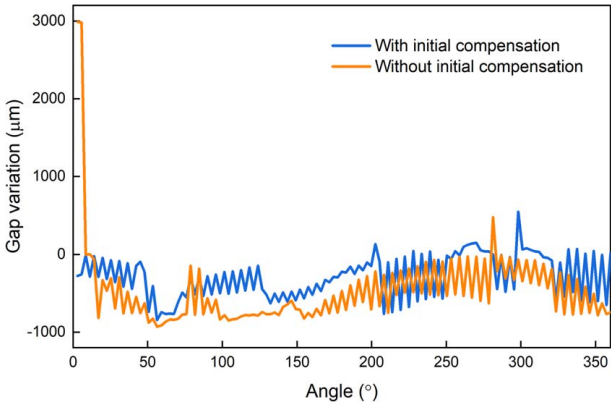

Fig. 10 Gap variations along paths for printing a circle on the test bed

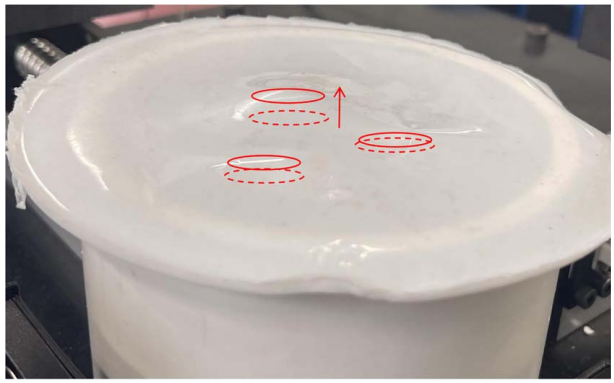

Fig. 11 Optical image of the deformable surface: the solid lines represent the current positions of the ball-shaped support and the dashed lines represent the initial flat positions of the support

respectively. z_0 is the coordinate of the initial point calculated in Sec. 4.2. After obtaining the final Z coordinate of the current point, we update this value to the input file of the manipulator to complete the compensation and printing of the point (Fig. 9). On average, the compensation calculation takes around 80 ms, while the manipulator is programmed to move every 0.5 s based on the ink extrusion rate. Consequently, the wait time for compensation calculation can be considered negligible.

To prevent instability the following two conditions should be enforced:

(1) $\dot{h}_s \Delta t_s \ll \Delta h$. Here $\dot{h}_s$ is the rate at which the surface can move up or down, Δt_s is the time for LDS to take the measurement and respond, and Δh is the difference between lowermost and uppermost nozzle positions for successful printing. This condition ensures that the surface does not move too fast to get the nozzle out of printing range before nozzle repositioning.

(2) $\dot{h}_s \ll \dot{h}_n$. Here $\dot{h}_s$ is the rate at which the surface can move up or down and $\dot{h}_n$ is the rate at which the nozzle can move. This condition ensures that the nozzle can move at a high enough speed to perform repositioning.

During the experiment, the sample rate of LDS is set to be 5 ms and the response time is 5 ms. The manipulator rate of change is approximately 0.7 mm/s. Thus, even under extreme conditions, when the actuator is moved to its maximum displacement, the system is fast enough to detect and react to avoid collision. In addition, we restrict the substrate's deformation range to not go beyond the manipulator's range of motion. In future work, we plan to explore methods to improve printing quality across varying surface distortions.

Although we have determined the Z-axis coordinates of the initial point in Sec. 4.2, the results may not be the optimal solution due to the limited resolution of the camera and the inaccuracy of the laser point size calculation. Therefore, we first perform initial compensation for the initial point in this section. In this process, the manipulator moves vertically in the Z-axis to find a suitable position without printing and then starts printing after the compensation is made. Figure 10 shows that after performing initial compensation, the gap's variations are decreased from approximately 521 μm to 276 μm when tracing circles and similar trends are observed on other geometries. Since the state of the test bed is random in each printing step, the trend of the gap can be different each time. It should be noted that the result of gap variation is the difference between the value detected by the LDS and the value we obtained during the initial point coordinate estimation. Therefore, the average of the gap variation is not zero. This also applies to the calculated results in Sec. 6.

5 Experimental Results

Two sets of experiments are performed in this paper: (1) testing the influence of the gap between the tooltip and the substrate; and (2) testing the efficacy of the proposed approach under different conditions.

We first test the influence of the gap, defined as the vertical distance between the end of the tooltip and the substrate, on the printing quality. This gap is found to be a key parameter for successful printing. In this experiment, the tool has an angle of 45 deg to the normal direction of the test bed. In this configuration, a relatively small gap (e.g., 34 μm) can cause discontinuous extrusion of ink (Fig. 8(*a*)). Due to the viscosity of the ink, a relatively large gap (e.g., 89 μm) can lead to the generation of ink droplets (Fig. 8(*c*)), and the laser point is easily illuminated on the surface of the droplet and reflected. In such a situation, the laser reading is the distance between the LDS and the ink droplet, which is almost a fixed value. This prevents correct calculation of the compensation using the sensor data. Based on a series of experiments, the appropriate gap is found to be approximately between 40 ± 5 μm to 70 ± 5 μm for continuous printing with line widths within the 730 μm to 800 μm range (Fig. 8(*b*)). Given the repeatability error of the manipulator, this sets the gap variation requirement. To test the effectiveness of the method, we print three different types of patterns, namely circles, squares, and spirals, on both static surfaces with different curvatures and deformable surfaces with gaps within the appropriate range determined by the above tests.

To print these patterns, we first project a circle, a square, or a spiral pattern orthogonally onto a horizontal plane. Then the printed trajectory of the manipulator is calculated based on the obtained graph, the TCP calibration, and the estimation of the initial point coordinates. Finally, the gap between the tooltip and the target surface is within the appropriate range. As shown in Fig. 12, both TCP calibration and gap compensation are necessary for the successful printing of complete patterns. The calibration process ensures that the position of the tooltip is near the laser point and can be approximated at the laser point so that the LDS reading used for the compensation calculation is based on the position of the tooltip. After the initial point estimation, the printing quality is improved. Finally, after the initial compensation for the initial point, we are able to successfully print complete patterns on deformable surfaces. The line widths of the patterns (circular, square, and spiral) printed on surfaces are measured using an optical microscope (Fig. 14). The line widths typically range from 900 μm to 1000 μm. As shown in Figs. 15 and 16, the same patterns can be created successfully on static surfaces with different curvatures. This method can be applied to both static and dynamic surfaces.

To assess the repeatability of our method, we first use basic lines as the reference geometry to examine the print continuity and line width on a static, flat surface. Lines are drawn on a stationary

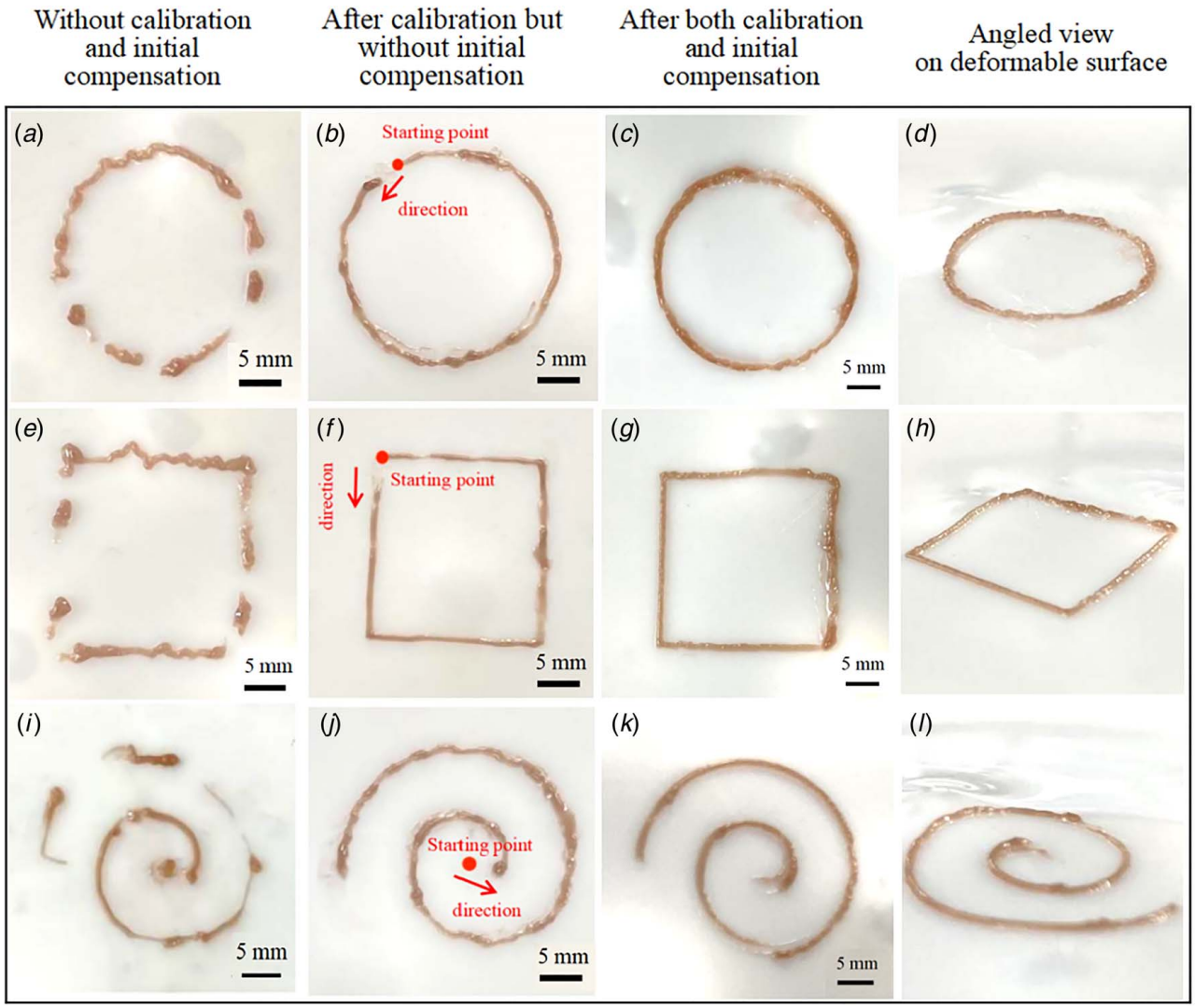

Fig. 12 Optical images of the printed patterns on the deformable surface: (*a*)–(*d*) circle, (*e*)–(*h*) square, (*i*)–(*l*) spiral. (*a*)–(*c*), (e)–(*g*), and (*i*)–(*k*) are top-down view directly and (*d*), (*h*), (*l*) are angled view of the printed patterns. All the images are taken directly from the test bed. (*a*), (e), (*i*) are prints without both calibration and initial compensation; (*b*), (*f*), (*j*) are prints after calibration but without initial compensation; and (c), (*g*), (*k*) are prints after applying both processes.

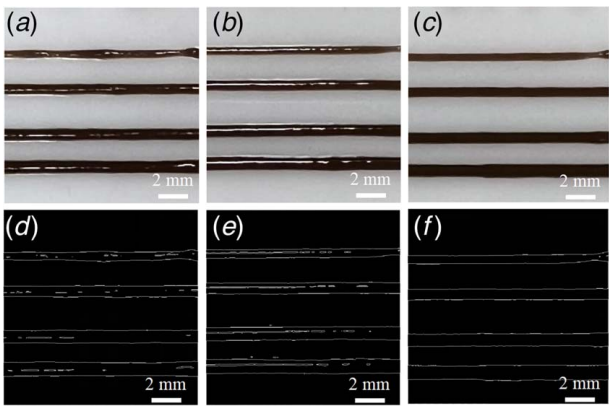

Fig. 13 Optical images illustrate the repeatability of the method with pressure increasing from top to bottom. Images (*a*)–(c) are the original captures of lines printed on a static, flat surface; images (*d*)–(e) show the processed images highlighting printing quality. Images (*a*) and (*d*) represent the initial prints conducted under identical experimental conditions; (*b*) and (e) were taken 5 min post the initial prints; (c) and (*f*) were captured 10 min following the initial prints.

plane at the start of the experiment, 5 min after the first test, and 10 min after the first test, under different air pressure conditions (Fig. 13). The results show that under the same experimental conditions, the widths of the lines show minimal variation at similar time points, approximately 779.76 μm, 881.64 μm, 903.99 μm, and 928.08 μm, respectively. Different shapes under a deterministic motion pattern are printed several times to test the printing consistency. Circle, spiral, and square are used as reference geometries to print five times respectively and the deformation conditions are all the same as shown in Fig. 4(*e*). In each trial, five points are selected randomly to evaluate the line width of the printed shapes. The results show that under a deterministic motion pattern, the line widths do not show much variation for all the shapes (see Table 1 for details).

6 Characterizing the Factors Affecting Gap Variation

6.1 Effect of Laser Point Position on Gap Variation. In previous work, we have characterized the effect of inaccuracy in the robot kinematic model on gap variation. In this paper, due to the small distance between the tooltip and the laser point, the compensation calculation is performed by scanning and detecting the area

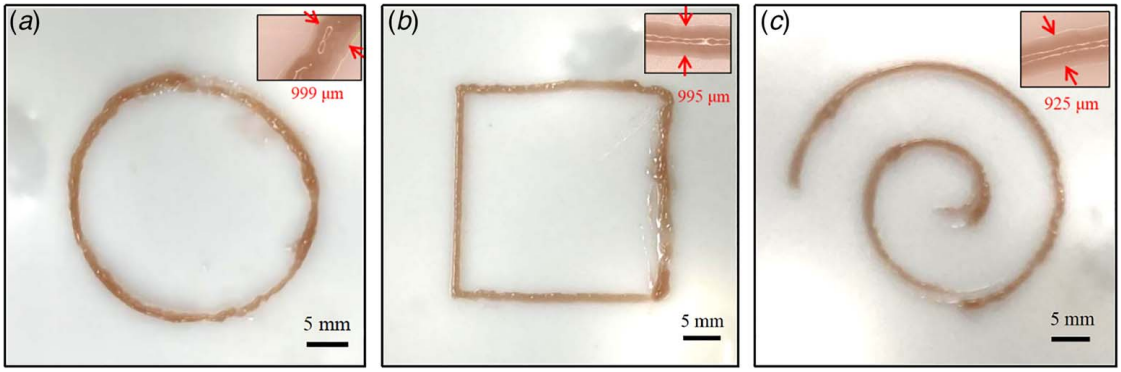

Fig. 14 Optical images of the printed patterns after both calibration and compensation on a deformable surface: (*a*) circle, (*b*) square, and (c) spiral. Insets show the measured line widths. The bright spot in the background is the head of the linear actuator.

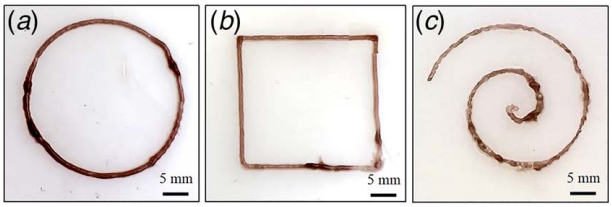

Fig. 15 Optical images of the printed patterns on a flat surface: (*a*) circle, (*b*) square, and (c) spiral

near the tooltip. In this process, the selection of regions may be one of the sources contributing to the variations in the gap.

We use basic lines as the reference geometry during this analysis. We have made shifts in the flange positions and orientation. Then we estimate the gap between the tooltip and the deformable surface. We evaluate the effect of different positions of laser point by the uniformity and thickness of the lines printed in the pattern and the numerical changes detected by the LDS. The results show that when the position of the laser point is always located at the next point on the trajectory of the current point of the tooltip (Fig. 17(*d*)), the variance of the gap variation is the smallest (approximately 104 μm) while the changes of gap variation in other positions are all approximately 260 μm (Fig. 18). This is reflected in the similar printing results shown in Fig. 17.

We did not change the orientation of the flange to improve the gap variation in the current work. The main reason is that the tooltip is not used as the center of the flange, though we can use the pattern to be printed, which is the trajectory of the tooltip, to inversely deduce the trajectory of the flange. However, this process is complicated. Through previous analysis, we found that the influence of the position of points detected by the laser point on gap variation is limited. In addition, the deformation of the surface is limited given the relatively small displacement and the speed of linear actuators. Despite successful deposition, the quality of the pattern on a surface of larger curvature is lower than that on a surface of smaller curvature due to the non-ideal fitting of the tooltip to the surface (Fig. 16(*g*)). In the future, we envision that a new algorithm can be developed to directly obtain the position of the flange, thereby allowing the direction and orientation of the tooltip to be changed in real-time during printing to further improve the quality of the patterns applicable to surfaces of different curvatures.

6.2 Effect of Target Surface Color on Gap Variation. Since the LDS is used to measure distances using the reflected laser beam,

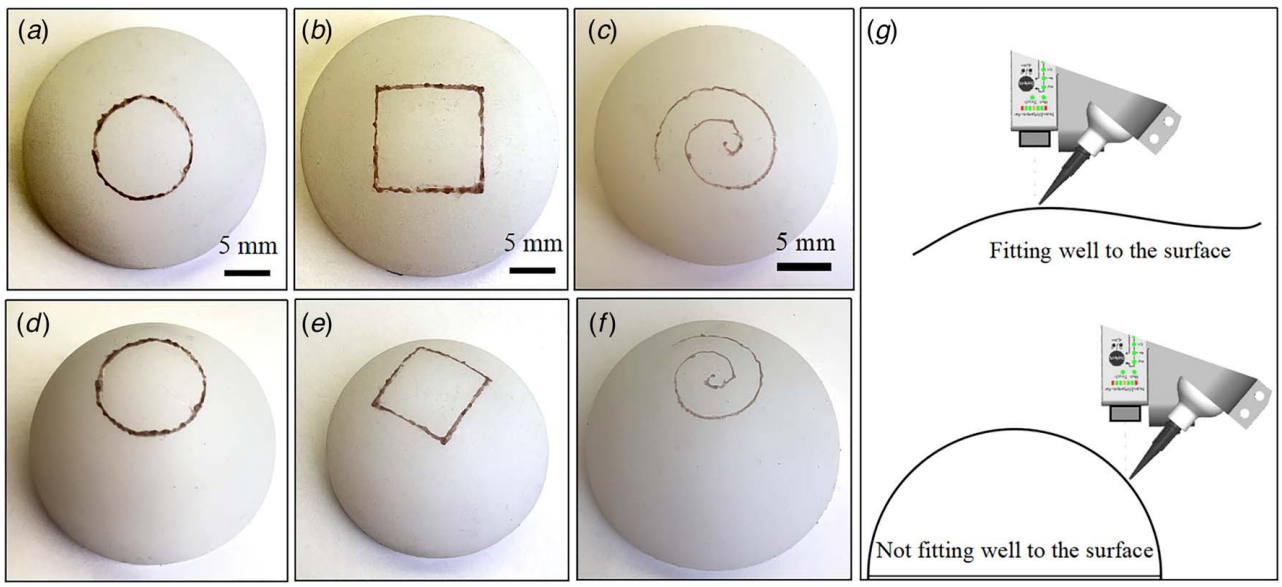

Fig. 16 Optical images of printed patterns on a static hemispherical surface: (*a*), (*d*) circle, (*b*), (*e*) square, and (c), (*f*) spiral. (*a*)–(c) are top-down view and (*d*)–(*f*) are angled view of the printed patterns, and (*g*) is the comparison of fitting to surfaces with different curvatures

Table 1 Line widths for different shapes under a deterministic motion pattern

	Circle		Square		Spiral	
Sample	Average (μm)	Standard deviation (μm)	Average (μm)	Standard deviation (μm)	Average (μm)	Standard deviation (μm)
1	933.56	37.93	953.14	43.96	953.66	25.70
2	953.90	28.60	936.84	27.18	930.44	11.44
3	958.10	36.33	907.70	29.15	979.08	9.98
4	933.54	25.25	950.98	43.35	971.82	34.67
5	984.42	57.26	955.14	31.53	980.44	17.55

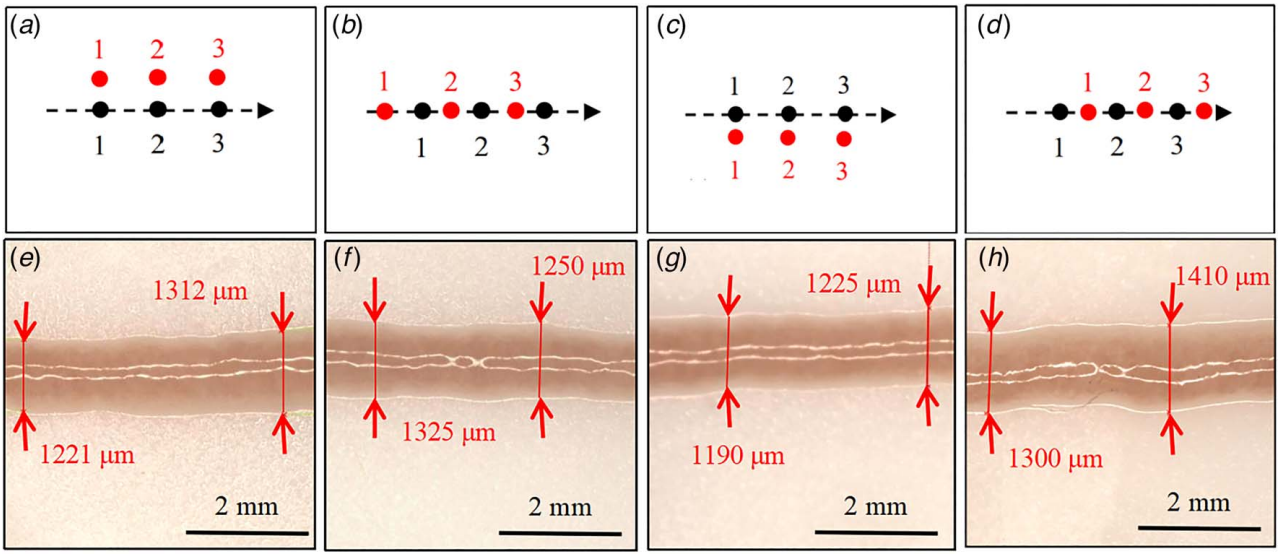

Fig. 17 Effect of laser point position on the printing results: (*a*)–(*d*) schematic illustrations of the relative position between the laser point and the tooltip. The black and red dots represent the tooltip and laser point, respectively. The numbers represent the order of the points, and (e)–(*h*) corresponding printing results for (*a*)–(*d*). (Color version online.)

the color of the target surface influences the accuracy of the measured lengths.

Circle, spiral, and square are used as the reference geometries for this analysis. We choose white, pink, and black colors by adding the corresponding dyes (Silc Pig, Smooth-On) as the membrane surface color. Then the gap between the tooltip and the surface is estimated. We evaluate the effect of different membrane surface colors using the numerical changes detected by the LDS (Fig. 19). The results show that the black color has a larger standard deviation value (approximately 427 μm) than the other two colors (approximately 350 μm for both pink and white). Although the error is within the acceptable range, brighter surfaces lead to higher accuracy during the experiment.

6.3 Effect of Laser Displacement Sensor Position on Gap Variation. The orientation of the LDS also influences the sensor reading on curved surfaces. In an initial experimental setup illustrated

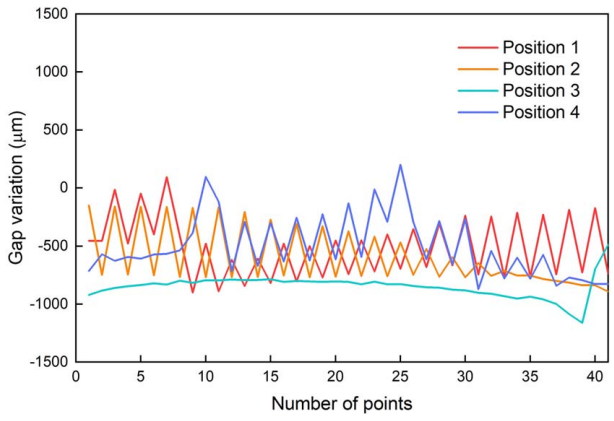

Fig. 18 Gap variations along paths for printing lines with different orientations on the test bed. Position number 1–4 corresponds to position number (*a*)–(*d*) in Fig. 17, respectively (Color version online.).

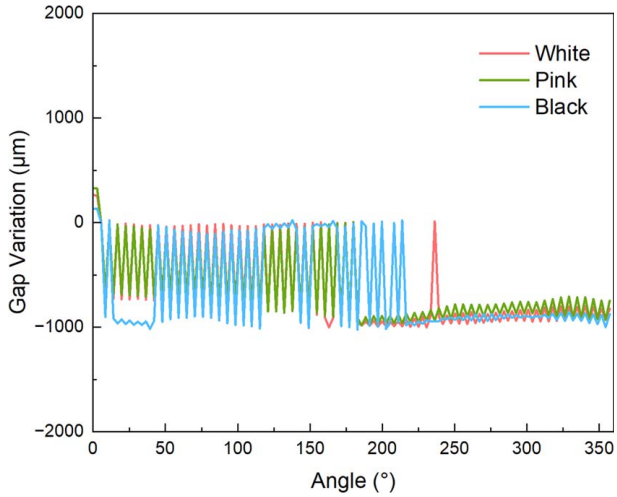

Fig. 19 Gap variations along paths for printing a circle on target surfaces in different colors (Color version online.)

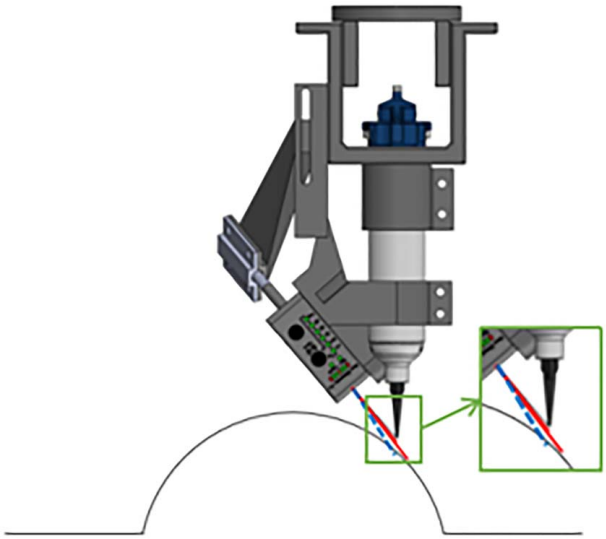

Fig. 20 Schematic illustration of the inaccuracy in LDS readings in an initial experimental setup. The solid line and the dashed line represent the actual laser beam and an imaginary laser beam for accurate gap measurement, respectively.

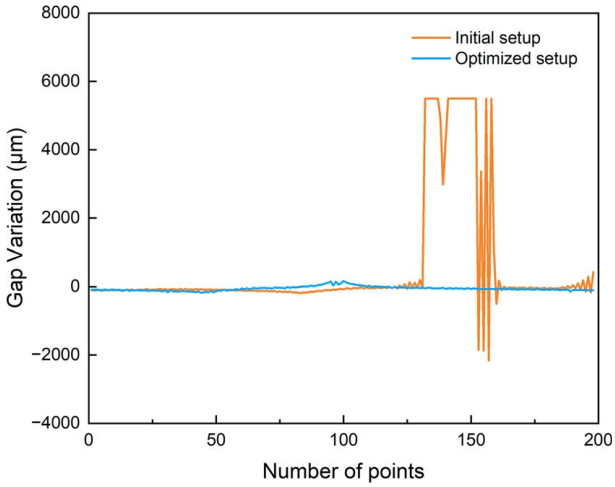

Fig. 21 Gap variations along paths for printing lines on a static curved surface in two different printing setup designs

in Fig. 20, the material deposition tool is perpendicular to the target surface and the LDS is at 45 deg to the surface. The constant flange orientation in this configuration can lead to inaccuracies in the LDS readings. More specifically, the LDS reading reflects the travel distance of the laser beam reflected from the curved surface (represented by the red solid line in Fig. 20, which does not accurately correspond to the distance between the tooltip and its vertical projection on the surface. This discrepancy likely contributes to the large gap variations shown in Fig. 21, affecting the compensation results. Consequently, this may lead to poor printing quality and potential damage to the target surface due to collisions with the tooltip.

In an optimized experimental setup used in this study, the LDS is perpendicular to the target surface and the material deposition is at an angle to the surface (Fig. 4). The angle is set to avoid collisions between any part of the tooltip and the surface during the entire printing process. The vertical orientation of the LDS ensures that changes in the LDS readings reflect the actual changes in the gap between the tooltip and the surface. We evaluate the influences of different experimental setups on the printing quality by drawing straight lines on a static curved surface. The optimized setup results in significantly reduced gap variations (Fig. 21).

It is important to note that the ranges of data for the characterization of gap variations due to the three factors in this section are different. This is due to the fact that the test beds used in Secs. 6.1 and 6.2 are real-time deformable surfaces, whereas Sec. 6.3 is a stationary curved plane.

7 Conclusions

Through the experiments above, we have demonstrated that industrial robotic manipulators can be used to perform conformal deposition on deformable surfaces through sensor-based planning and control. The main research results of this paper are summarized as follows:

(1) By using a 6-DOF manipulator with multiple sensors, including the LDS and cameras, we realized printing different patterns on a deformable surface with line widths within 800–1000 μm;
(2) By exploiting the high repeatability of the manipulator and the LDS, we demonstrated that the gap variation can be reduced to approximately 200 μm by using the proposed compensation scheme;
(3) Through experiments, we investigated the sources of gap variations. This can be used in the future to apply advanced methods to further improve the printing quality.

The approach presented in this study provides a relatively simple means of achieving conformal deposition on deformable surfaces based on sensor planning and control. The results show the possibility of conformal printing on dynamically changing surfaces, which may find applications in fabricating bioscaffolds for tissue regeneration, advanced sensors on complex surfaces, and patient-specific wearable and implantable devices. Future work will focus on understanding how various parameters—including temperature, surface deformation rate, ink extrusion rate, among others—impact the quality of printing, as well as reducing printing errors by improving the manipulator's positioning accuracy, adjusting the tool orientation to be ahead of the tooltip, and applying AI to detect, adapt, and predict the state of the printing environment.

Acknowledgment

This work is supported by the Center for Advanced Manufacturing at the University of Southern California.

Conflict of Interest

There are no conflicts of interest.

Data Availability Statement

The datasets generated and supporting the findings of this article are obtainable from the corresponding author upon reasonable request.

References

[1] Gibson, I., Rosen, D. W., and Stucker, B., 2010, *Additive Manufacturing Technologies: Rapid Prototyping to Direct Digital Manufacturing*, Springer, New York.
[2] Shembekar, A. V., Yoon, Y. J., Kanyuck, A., and Gupta, S. K., 2019, "Generating Robot Trajectories for Conformal Three-Dimensional Printing Using Nonplanar Layers," ASME J. Comput. Inf. Sci. Eng., **19**(3), p. 031011.
[3] Zhang, G. Q., Mondesir, W., Martinez, C., Li, X., Fuhlbrigge, T. A., and Bheda, H., 2015, "Robotic Additive Manufacturing Along Curved Surface – A Step Towards Free-Form Fabrication," International Conference on Robotics and Biomimetics (ROBIO), Zhuhai, China, Dec. 6–9, IEEE, pp. 721–726.
[4] Alsharhan, A. T., Centea, T., and Gupta, S. K., 2017, "Enhancing Mechanical Properties of Thin-Walled Structures Using Non-Planar Extrusion Based

Additive Manufacturing," ASME 12th International Manufacturing Science and Engineering Conference Collocated With the JSME/ASME 2017 6th International Conference on Materials and Processing, American Society of Mechanical Engineers.
[5] Zhao, G., Ma, G., Feng, J., and Xiao, W., 2018, "Nonplanar Slicing and Path Generation Methods for Robotic Additive Manufacturing," Int. J. Adv. Manuf. Technol., **96**(9-12), pp. 3149–3159.
[6] Bhatt, P. M., Malhan, R. K., Shembeka, A. V., Yoon, Y. J., and Gupta, S. K., 2020, "Expanding Capabilities of Additive Manufacturing Through Use of Robotics Technologies: A Survey," Addit. Manuf., **31**, p. 100933.
[7] Bhatt, P. M., Kabir, A. M., Malhan, R. K., Shah, B. C., Shembekar, A. V., Yoon, Y. J., and Gupta, S. K., 2019, "A Robotic Cell for Multi-resolution Additive Manufacturing," IEEE International Conference on Robotics and Automation., Montreal, QC, Canada, May 20–24.
[8] Yoon, Y. J., Shembekar, A. V., Almeida, O. G., and Gupta, S. K., 2020, "A Robotic Cell for Embedding Prefabricated Components in Extrusion-Based Additive Manufacturing," ASME Manufacturing Science and Engineering Conference, Virtual, Sept. 3.
[9] Cai, Y., Bhatt, P. M., Zhao, H., and Gupta, S. K., 2022, "Using an Articulated Industrial Robot to Perform Conformal Deposition With Mesoscale Features," ASME Manufacturing Science and Engineering Conference, West Lafayette, IN, June 27–July 1.
[10] Gao, W., Zhang, Y., Nazzetta, D. C., Ramani, K., and Cipra, R. J., 2015, "RevoMaker: Enabling Multi-directional and Functionally-Embedded 3D Printing Using a Rotational Cuboidal Platform," Proceedings of the 28th Annual ACM Symposium on User Interface Software & Technology, Charlotte, NC, Nov. 8–11, ACM, pp. 437–446.
[11] Song, X., Pan, Y., and Chen, Y., 2015, "Development of a Low-Cost Parallel Kinematic Machine for Multidirectional Additive Manufacturing," ASME J. Manuf. Sci. Eng., **137**(2), p. 021005.
[12] Bhatt, P. M., Gong, C., Kabir, A. M., Malhan, R. K., Shah, B. C., and Gupta, S. K., 2020, "Incorporating Tool Contact Considerations in Tool-Path Planning for Robotic Operations," ASME Manufacturing Science and Engineering Conference, virtual, Sept. 3.
[13] Zhu, Z., Park, H. S., and McAlpine, M. C., 2020, "3D Printed Deformable Sensors," Sci. Adv., **6**(25), p. eaba5575.
[14] Neto, P., 2013, "Off-line Programming and Simulation From CAD Drawings: Robot-Assisted Sheet Metal Bending," IECON 2013 – 39th Annual Conference of the IEEE Industrial Electronics Society, Vienna, Austria, Nov. 10–13, pp. 4235–4240.
[15] Perumaal, S. S., and Jawahar, N., 2013, "Automated Trajectory Planner of Industrial Robot for Pick-and-Place Task," Int. J. Adv. Rob. Syst., **10**(2), p. 100.
[16] Kabir, A. M., Langsfeld, J. D., Zhuang, C., Kaipa, K. N., and Gupta, S. K., 2016, "Automated Learning of Operation Parameters for Robotic Cleaning by Mechanical Scrubbing," ASME 11th International Manufacturing Science and Engineering Conference, Vol. 2, Blacksburg, VA, June 27–July 1.
[17] Langsfeld, J. D., Kabir, A. M., Kaipa, K. N., and Gupta, S. K., 2018, "Integration of Planning and Deformation Model Estimation for Robotic Cleaning of Elastically Deformable Objects," IEEE Rob. Autom. Lett., **3**(1), pp. 352–359.
[18] Cai, Y., Han, Z., Cranney, T., Zhao, H., and Gupta, S. K., 2021, "Automated Robotic Assembly of 3D Mesostructure Via Guided Mechanical Buckling," 2021 IEEE 17th International Conference on Automation Science and Engineering (CASE), Lyon, France, Aug. 23–27, IEEE, pp. 2098–2104.
[19] Wang, X., Xue, L., Yan, Y., and Gu, X., 2017, "Welding Robot Collision-Free Path Optimization," Appl. Sci., **7**(2), p. 89.
[20] Chidhambara, K. V., Shankar, B. L., and Vijaykumar, 2018, "Optimization of Robotic Spray Painting Process Parameters Using Taguchi Method," IOP Conf. Ser.: Mater. Sci. Eng., **310**(1), p. 012108.
[21] Bhatt, P. M., Kabir, A. M., Malhan, R. K., Shah, B., Shembekar, A. V., Yoon, Y. J., and Gupta, S. K., 2019, "A Robotic Cell for Multi-resolution Additive Manufacturing," 2019 International Conference on Robotics and Automation (ICRA), Montreal, QC, Canada, May 20–24, IEEE, pp. 2800–2807.
[22] Urhal, P., Weightman, A., Diver, C., and Bartolo, P., 2019, "Robot Assisted Additive Manufacturing: A Review," Rob. Comput. Integr. Manuf., **59**, pp. 335–345.
[23] Xiong, J., Yin, Z., and Zhang, W., 2016, "Closed-loop Control of Variable Layer Width for Thin-Walled Parts in Wire and Arc Additive Manufacturing," J. Mater. Process. Technol., **233**, pp. 100–106.
[24] Zhang, Z., Zhao, Z., Zhang, Y., and Liu, S., 2022, "Multi-process Logistics Planning for Cost Minimization and Workload Balance in Steel Production Systems," 2022 IEEE International Conference on Networking, Sensing and Control (ICNSC), Shanghai, China, Dec. 15–18, pp. 1–6.
[25] Adams, J. J., Duoss, E. B., Malkowski, T. F., Motala, M. J., Ahn, B. Y., Nuzzo, R. G., Bernhard, J. T., and Lewis, J. A., 2011, "Conformal Printing of Electrically Small Antennas on Three-Dimensional Surfaces," Adv. Mater., **23**(11), pp. 1335–1340.
[26] Schaffner, M., Rühs, P. A., Coulter, F., Kilcher, S., and Studart, A. R., 2017, "3D Printing of Bacteria Into Functional Complex Materials," Sci. Adv., **3**(12), p. eaao6804.
[27] Su, R., Wen, J., Su, Q., Wiederoder, M. S., Koester, S. J., Uzarski, J. R., and McAlpine, M. C., 2020, "3d Printed Self-Supporting Elastomeric Structures for Multifunctional Microfluidics," Sci. Adv., **6**(41), p. eabc9846.
[28] Bhatt, P. M., Kulkarni, A., Malhan, R. K., Shah, B. C., Yoon, Y. J., and Gupta, S. K., 2022, "Automated Planning for Robotic Multi-resolution Additive Manufacturing," ASME J. Comput. Inf. Sci. Eng., **22**(2), p. 021006.
[29] Johnson, R. A., O'Neill, J. J., Dockter, R. L., and Kowalewski, T. M., 2017, "Toward Inkjet Additive Manufacturing Directly Onto Human Anatomy," Vol. 2017 Design of Medical Devices Conference of Frontiers in Biomedical Devices.
[30] O'Neill, J. J., Johnson, R. A., Dockter, R. L., and Kowalewski, T. M., 2017, "3D Bioprinting Directly Onto Moving Human Anatomy," 2017 IEEE/RSJ International Conference on Intelligent Robots and Systems (IROS), Vancouver, BC, Canada, Sept. 24–28, IEEE, pp. 934–940.
[31] Zhu, Z., Guo, S.-Z., Hirdler, T., Eide, C., Fan, X., Tolar, J., and McAlpine, M. C., 2018, "3D Printed Functional and Biological Materials on Moving Freeform Surfaces," Adv. Mater., **30**(23), p. 1707495.
[32] Zhu, Z., Ng, D. W. H., Park, H. S., and McAlpine, M. C., 2021, "3D-Printed Multifunctional Materials Enabled by Artificial-Intelligence-Assisted Fabrication Technologies," Nat. Rev. Mater., **6**(1), pp. 27–47.
[33] Kraljić, D., and Kamnik, R., 2018, "Trajectory Planning for Additive Manufacturing With a 6DOF Industrial Robot," International Conference on Robotics in Alpe-Adria Danube Region, Patras, Greece, June 6–8, Springer, pp. 456–465.
[34] Bhatt, P. M., McNulty, Z., and Gupta, S. K., 2022, "Robot Trajectory Generation for Multi-axis Wire Arc Additive Manufacturing," ASME Manufacturing Science and Engineering Conference., West Lafayette, IN, June 27–July 1.
[35] Holness, F. B., and Price, A. D., 2016, "Robotic Extrusion Processes for Direct Ink Writing of 3D Conductive Polyaniline Structures," *Electroactive Polymer Actuators and Devices (EAPAD) (International Society for Optics and Photonics*, Vol. 9798, Y. Bar-Cohen and F. Vidal, eds., SPIE, Washington, DC, p. 97981G.
[36] Jin, Y., Du, J., He, Y., and Fu, G., 2017, "Modeling and Process Planning for Curved Layer Fused Deposition," Int. J. Adv. Manuf. Technol., **91**(1–4), pp. 273–285.
[37] Lim, S., Buswell, R. A., Valentine, P. J., Piker, D., Austin, S. A., and De Kestelier, X., 2016, "Modelling Curved-Layered Printing Paths for Fabricating Large-Scale Construction Components," Addit. Manuf., **12**(B), pp. 216–230.
[38] Kim, C., Espalin, D., Cuaron, A., Perez, M. A., Lee, M., MacDonald, E., and Wicker, R. B., 2015, "Cooperative Tool Path Planning for Wire Embedding on Additively Manufactured Curved Surfaces Using Robot Kinematics," ASME J. Mech. Rob., **7**(2), p. 021003.
[39] Pratt, V., 1987, *Direct Least-Squares Fitting of Algebraic Surfaces*, Vol. 21, ACM, New York, NY, pp. 145–152.